PAPER

Check for updates

Shaped inorganic–organic hybrid catalysts based on solid molecular catalysts for continuous formic acid dehydrogenation

Sebastian Seidel, [ID] [a] Keanu V. A. Birkelbach, [ID] [a] J. Mädicke,[a] M. Pilaski, [ID] [b] Peter J. C. Hausoul [ID] [a] and Regina Palkovits [ID] *[a]

A synthetic methodology for the immobilization of solid molecular catalysts (SMCs) in cylindrically shaped porous glass substrates was developed to facilitate their use in a continuous plug-flow reactor. The glass supports were coated with tailor-made alkoxysilanes to enable covalent attachment of, 'in pore' polymerized SMCs. Inorganic–organic hybrid catalysts based on BINAP-, terpyridine- and triazine were successfully prepared and tested in formic acid dehydrogenation after impregnation with 0.1 wt% Ru or Ir. In a plug-flow reactor, TOFs of up to 11 500 h^{-1} and selectivities of 75 ppm CO could be observed at 160 °C, while at 100 °C the activity remained at 6200 h^{-1} with a CO concentration of 79 ppm.

Introduction

Enabling a sustainable chemical industry requires the efficient utilization of limited resources.[1] Reducing the use of precious metals (*e.g.* Ru, Ir, Pd or Pt) and adopting renewable carbon feed streams such as CO_2 over fossil-based resources are key in achieving this. Due to climate change and the envisioned fade-out of fossil fuels, the use of renewable energy sources is also on the rise.[2] Given seasonal and regional fluctuations in renewable energy production, large-scale energy storage technologies will need to be developed and deployed until 2050.[3] One such technology is the storage of hydrogen generated by water electrolysis in liquid hydrogen carriers (LHCs) such as MeOH, liquefied NH_3 or formic acid (FA).[4–10]

A strategy unifying these concepts is the utilization of solid molecular catalysts (SMCs) for the synthesis of formic acid from CO_2 and H_2 as well as formic acid dehydrogenation (FAD) to release H_2 on demand. SMCs combine the high activity of homogeneous catalysts and the straightforward handling and recycling of heterogeneous catalysts and thus offer unique advantages for technical applications.[14,15] To date, several different immobilization strategies, including covalent attachment, ionic interactions and adsorption, have been developed (see Table S2 for a more detailed comparison).[14–22] For FAD, immobilized catalysts, based on surface-grafted silica (Fig. 1) were reported as early as 2009.

Gan *et al.* reported a Ru(TPPTS)L$_4$@PPh$_2$(CH$_2$)$_n$/SiO$_2$ catalyst with turnover frequencies (TOFs) of up to 2780 h^{-1} at 110 °C in 13 wt% aqueous FA. Another notable silica immobilized catalyst is the IrH$_3$@PN^{3}P/SiO$_2$ pincer catalyst reported by Alrais *et al.* While utilizing a mixture of FA and caesium formate at 90 °C, a TOF of up to 13 290 h^{-1} and a turnover number (TON) of up to 540 000 were obtained.[12] In addition, several noble-metal-free immobilized catalysts have been reported in recent years, decreasing the economic burden of the catalytically active material at the cost of more sophisticated ligand synthesis. One prominent example is the Fe(BF$_4$)$_2$@polyRPhphos/SiO$_2$ catalyst reported by Stathi *et al.*[13] It exhibits TOFs of up to 7600 h^{-1} and TONs of up to 8500 in the decomposition of 40 wt% FA in propylene carbonate at 90 °C. The technical application of catalysts supported on SiO$_2$ is usually limited by the stability of the support towards solvents, acidic or basic conditions and subsequent leaching of the ligand and metal species in continuous operation.[23]
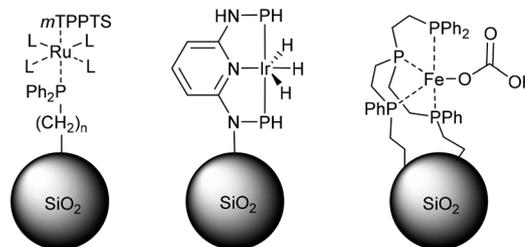

Fig. 1 Examples of molecular catalysts immobilized on SiO$_2$ (left: Ru(TPPTS)@PPh$_2$(CH$_2$)$_n$/SiO$_2$,[11] middle: IrH$_3$@PN^{3}P/SiO$_2$,[12] and right: Fe(BF$_4$)$_2$@polyRPhphos/SiO$_2$ [13]).

[a] Institut für Technische und Makromolekulare Chemie, RWTH Aachen University, Worringerweg 2, 52074 Aachen, Germany. E-mail: Palkovits@itmc.rwth-aachen.de
[b] ZBT - Zentrum für Brennstoffzellentechnik GmbH, Carl-Benz-Straße 201, 47057 Duisburg, Germany

This journal is © The Royal Society of Chemistry 2026

Catal. Sci. Technol., 2026, **16**, 2129–2138 | **2129**

Several highly active SMCs were reported based on fully organic covalent triazine frameworks (CTFs), covalent organic frameworks as well as polyaromatic frameworks, circumventing the degradation of the catalysts under acidic conditions (Fig. 2).[24–32] Organic macromolecular systems often exhibit a pronounced swelling behaviour. Furthermore, shaping of such catalyst materials for industrial application remains largely unstudied.[33] Depending on the material, several strategies for shaping are viable. Materials can be shaped into monoliths during or after synthesis by using pressure or a binder and subsequently cutting or grinding them to the required shape.[34]

Another option is coating the surface of a rigid support such as silica, glass or zeolite with the active catalyst phase, to yield inorganic–organic hybrid catalysts.[28] The latter has previously been investigated by Bavykina et al. for CTF systems supported on cordierite monoliths for FAD of 3 M aqueous FA with TOFs of up to 207 000 h^{−1} at 80 °C in a continuously stirred tank reactor (CSTR).[28–35] Several further continuous reaction systems for FAD have previously been reported in literature. Ruiz-López et al. describe a CSTR for liquid-phase FAD with bimetallic PdRu particles (5 wt% RuPd/C_3N_4) supported on graphitic carbon nitride, exhibiting a TOF of 30 h^{−1} and a TON of 60 for the decomposition of 1 M aqueous FA at 60 °C.[36] Sponholz et al. developed a homogeneous reactor system based on $RuCl_2$-bis(1,2-bis(diphenylphosphino)ethane), which, in a CSTR with connected gas purification and the addition of N,N-dimethyloctylamine as an activating base, exhibited a TOF of 1000 h^{−1} over a reaction time of 45 days (TON = 1 000 000) at 25 °C.[37] By increasing the amount of FA added and the temperature to 60 °C, this system achieved a TOF of 16 000 h^{−1} at 6.5 bar. Sawahara et al. previously reported a Cp*Ir@PEI flow reaction system capable of FAD of 20 M aqueous FA at 80 °C using a syringe pump with a TON of 332 000 over 2100 h and CO concentrations of below 0.1 ppm.[38]

Here we present the preparation of shaped hybrid inorganic–organic catalysts via surface modification and in-pore Suzuki coupling of catalytically active phase in porous borosilicate cylinders. Three different catalysts based on Ru/BINAP, Ir/terpyridine and Ir/CTF are prepared and compared in batch formic acid dehydrogenation reactions. To de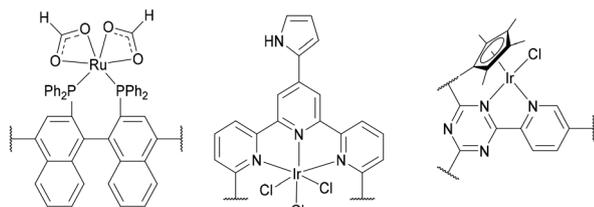monstrate the applicability of the approach as well as long term stability of the catalyst, the best performing system is investigated using a continuous plug flow reactor.

Results and discussion

Surface modification and Suzuki post functionalization of silica

For the synthesis of covalently bound inorganic–organic hybrid catalyst materials, supports such as borosilicate glass or silica were first coated with silanes containing functional groups that are subsequently used in Suzuki coupling reactions. To this end, electrophilic halo- or alkoxysilanes can be coupled to the support by a DMF catalysed condensation reaction in toluene, as previously published by Chiang et al. (Fig. 3).[39–41]

Silica support (Saint Gobain) was ground to a powder and subsequently coated with the silanes trimethylsilyl chloride (TMSCl) (TMS@SIO_2), trimethoxyphenylsilane (PhSi(OMe)$_3$) or triethoxy-(4-bromophenyl)silane (BrPhSi(OEt)$_3$).[42,43] The specific surface area (SSA) of the utilized SiO_2 remained comparable with 228 m[2] g^{−1} for the unmodified material and 223 m[2] g^{−1} for BrPh@SiO_2. After the reaction, the DRIFTS spectrum (Fig. 4, left) of TMS@SiO_2 exhibits the expected signals at 2970 cm^{−1}, corresponding to stretching vibration modes of C–H bonds in surface –CH_3 groups formed during the silylation process.[44,45]

Coating with PhSi(OMe)$_3$ leads to additional signals corresponding to $C_{arom.}$–$C_{arom.}$ at 1433 cm^{−1} and 1595 cm^{−1}, as well as $C_{arom.}$–H vibration bands at 3060 cm^{−1} and 3077 cm^{−1} thus validating the coating procedure.[46] Usage of the target silane BrPhSi(OEt)$_3$ leads to a vibration band at 1580 cm^{−1}, attributed to a C–C stretching vibration mode (Fig. S1 and S2).[47] Additionally, a band emerges at 1486 cm^{−1}, also attributed to BrPhSi(OEt)$_3$. Subsequently, solid state magic angle spinning (MAS) ^{29}Si NMR (Fig. 4, middle) was employed to further elucidate the structure of BrPh@SiO_2. In addition to the Q^n-type Si(OSiO$_3$)$_n$(R)$_{4−n}$ signals (Q^2 = −92 ppm, Q^3 = −100 ppm and Q^4 = −110 ppm) exhibited by the unmodified silica material, a T^n-type silicon signal at T^3 = −67 ppm Si(OSiO$_3$)$_n$(R)$_{3−n}$ corresponding to the BrPhSi(OEt)$_3$ coating could be observed.[41,48] ^{13}C NMR reveals the signals expected for BrPhSi(OEt)$_3$ at 125 ppm, 130 ppm and 134 ppm (Fig. 4, right). Additionally, signals can be observed at 16 ppm and 57 ppm resulting from residual ethoxy groups, suggesting incomplete coupling of BrPhSi(OEt)$_3$ to the surface. XRD reveals no significant change due to the coating (Fig. S3).

A subsequent Suzuki-cross coupling reaction was explored as a pathway to post-functionalize the surface-bound fragments. Due to the lability of the model support SiO_2 towards the basic conditions during the reaction, protection of the surface was achieved by treating the BrPhSi(OEt)$_3$ modified support (BrPh@SiO_2) with TMSCl and washing with EtOH (TMS + BrPh@SiO_2). This led to an additional signal in the ^{29}Si-SS-NMR (Fig. 4, middle) at 15 ppm with a concurrent decrease in the Q^2 signal at −92 ppm and a relative increase
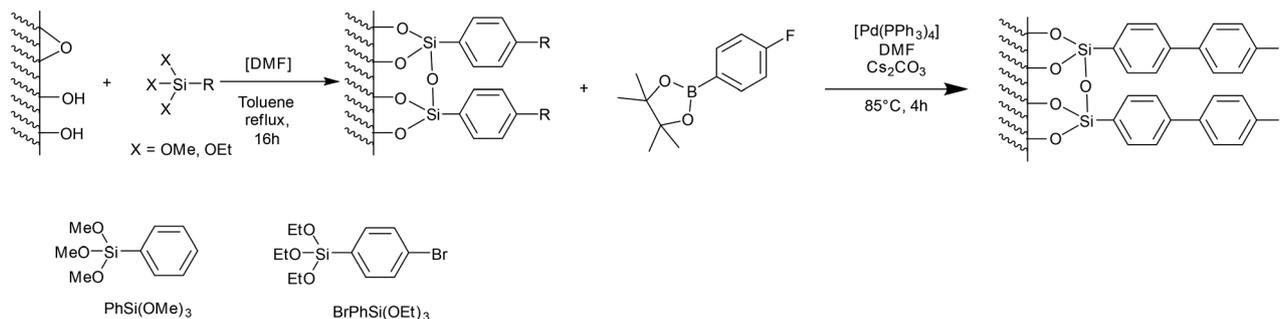

Fig. 2 Ru(FA)$_2$@pBINAP (left), IrCl$_3$@PyrTerpy and Ir(Cp*)Cl@CTF by Gascon et al.[24]

Fig. 3 Coating procedure of SiO$_2$ with alkoxysilanes (PhSi(OMe)$_3$ and 4–BrPhSi(OEt)$_3$) and subsequent Suzuki coupling of surface grafted BrPh@SiO$_2$ with 4-fluoro phenyl pinacol.
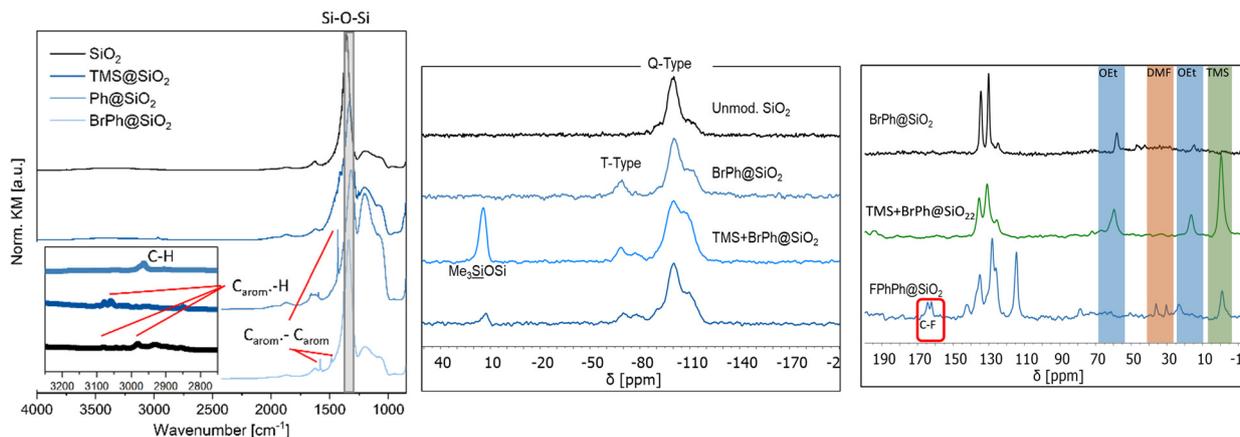

Fig. 4 DRIFTS (left, inset: zoom on CH-region of the three modified materials), solid-state ^{29}SI (middle) and ^{13}C (right) NMR spectra of pristine SiO$_2$, TMS@SiO$_2$, Ph@SiO$_2$ and BrPh@SiO$_2$.

in the Q^4 signal at −110 ppm. This is in line with the behaviour expected for a subsequent protection of exposed Si atoms with TMSCl.[49] ^{13}C NMR (Fig. 4, bottom) reveals a relative increase in the residual ethoxy signals at 16 ppm and 57 ppm, attributed to a acidic ethoxylation of free surface silanol groups. Subsequently, the silane-functionalized material was coupled with 2-(4-fluorophenyl) pinacol boron ester at 85 °C in DMF. The structure of the resulting material was investigated using DRIFTS spectroscopy, ^{13}C, ^{19}F as well as ^{29}Si NMR. In ^{29}Si NMR a decrease of the TMS signal can be observed which is attributed to base induced hydrolytic cleavage of the support. This is underlined by the decrease in the signal of the base labile surface bound ethoxy groups observed in ^{13}C NMR. Nonetheless, the signal attributed to a T^3-type aromatic silicon atom can be observed at −67 ppm. ^{13}C NMR reveals additional signals at 165 ppm, 140 ppm and 115 ppm attributed to the 4-fluorobiphenyl moieties. In ^{19}F NMR, a broad signal at −120 ppm can be attributed to the surface bound 4-fluorobiphenyl, whereas a sharp peak at −115 ppm represents unreacted substrate adsorbed to the surface (Fig. S5). This confirms that Suzuki cross-coupling can be successfully applied to a surface functionalized silica, albeit with some loss of the functional group density.

Surface modification and Suzuki post functionalization of borosilicate glass

The functionalization and post modification method was also investigated for the more robust borosilicate glasses. These are commercially available as porous pellets and cylinders in various sizes and porosities, enabling fine tuning of support properties. Due to the shape and high surface roughness of the targeted cylindrical porous glass supports, direct spectroscopic characterisation of these coated materials proved to be challenging. To still allow spectroscopic insight, ball-milled porous glass was grafted with the target silanes after a thorough cleaning procedure using Piranha acid (conc. H$_2$SO$_4$: 36% H$_2$O$_2$ 7:3) and Piranha base (36% H$_2$O$_2$: 30% NH$_4$OH : H$_2$O 1:1:5) using the procedure described for the silica materials.[39]

DRIFTS spectra of the coated materials show no significant change in comparison to the spectra of unmodified material (Fig. S6). Analysis of the resulting glass using ^{29}Si NMR was performed and revealed one broad signal at −100 ppm attributed to the bulk material (Fig. S7).[50,51] Additionally, a weak shoulder between −70 ppm and −85 ppm can be observed, which is attributed to a surface bound T-type organosilane. No exact structure determination was

possible due to the overall low fraction of reactive surface Si atoms in comparison to the inaccessible silicon in the bulk material due to the low surface area of the shaped glass supports.

In addition, commercially available microscope slides were coated accordingly to allow characterization *via* ATR-IR (Fig. 5). The strong band near 910 cm^{-1} is attributed to the asymmetric stretching vibration of BØ$_4$-tetrahedra (Ø denotes a bridging oxygen atom).[52–54] In the region below 900 cm^{-1}, deformation modes are found and attributed to the various constituents of the network such as B–O–B and Si–O–Si bridges or mixed Si–O–B. The spectrum for BrPh@glass differs from pristine glass by very weak additional ν(C–C) bands at 1579 cm^{-1} as well as 1483 cm^{-1} which are attributed to the coating with BrPhSi(OEt)$_3$ and were previously observed for BrPh@SiO$_2$.

To further verify the successful silane coating on glassy supports, the contact angle with H$_2$O was measured for the different silane coatings as well as uncoated glass (Fig. S8). Unmodified glass exhibits a low contact angle of 29.8°, in line with a hydrophilic surface featuring Si–OH groups.[40] After coating with TMSCl, an angle of 99.8° was observed, demonstrating a decreased hydrophilicity. After coating the surface with PhSi(OMe)$_3$ a contact angle of 89.8° was observed, while the BrPhSi(OEt)$_3$ coating active in Suzuki-coupling reactions leads to a contact angle of 100.0°. Thus, it could be shown that the surface coating method proceeds successfully for all the studied glasses.

Synthesis of inorganic–organic hybrid catalyst materials

The synthesis of inorganic–organic hybrid catalyst materials was carried out using a procedure previously developed by our group based on a Suzuki cross coupling reaction.[55] After surface activation of the porous glass supports using BrPhSi(OEt)$_3$ as described above, a solvothermal synthesis procedure was carried out in a tubular autoclave under

Fig. 5 ATR-IR spectrum of cleaned microscope slides before coating (top) and glass surface-coated with BrPhSi(OEt)$_3$. Insert: Magnified C–C vibrational area of ATR-IR spectrum.

Schlenk conditions. The use of cylindrical porous glass facilitates catalyst utilization in a plug-flow-reactor (Fig. S9).

Three supported porous polymeric catalyst systems were obtained by polymerization of three different monomers and subsequent metal loading (Fig. 6): 1.) 5,5′-dibromo-2,2′-bis(diphenylphosphino)-1,1′-binaphthyl (BINAPO), yielding a ruthenium/polyphosphine catalyst (Ru@pBINAP/G),[56] 2.) 6,6″-dibromo-4′-(1*H*-pyrrol-2-yl)-2,2′-6′,2″-terpyridine, yielding a iridium/terpyridine-based solid molecular catalyst (Ir@PyrTerpy/G),[56] 3.) 2,4,6-tris(4-(pinacol boron ester) phenyl)-1,3,5-triazine yielding a CTF-type supported iridium catalyst (Ir@CTF/G).[57]

Due to insufficient solubility of the monomers in the solvent DMF, the porous support was pre-loaded with the respective polymerisation solution in DMF by incipient wetness impregnation. Thereby, a sufficient amount of [Pd(PPh$_3$)$_4$] and Cs$_2$CO$_3$ in addition to the monomers could be introduced into the cylindrical or pelletized porous borosilicate supports under argon flow. After 72 h at 85 °C the resulting crude hybrid supports were obtained. Following an oxidative cleaning procedure utilizing H$_2$O$_2$/HCl to remove Pd(0) leftover in the organic fraction, further processing was performed depending on the organic coating. In the case of Ru@pBINAP/G, the BINAP oxide containing material, this involved the reduction of the phosphine oxides to phosphines by transfer (de)oxygenation using PPh$_3$/HSiCl$_3$.[58] After washing with toluene to remove leftover PPh$_3$ and subsequent impregnation with Ru(methyl-allyl)$_2$COD (0.1 wt%), Ru@pBINAP/G could be obtained as a yellow-beige shaped hybrid catalyst. The metal uptake for all materials was investigated using ICP of the metal solution after filtration a loading of 0.065 wt% was found for Ru@pBINAP/G (Table 1). Analogously, Ir@PyrTerpy/G was obtained after the polymerisation and oxidative treatment by wet impregnation with IrCl$_3$·H$_2$O in MeOH (0.087 wt% Ir uptake) without prior reduction as a yellow to orange solid. Ir@CTF/G was obtained after polymerisation by wet impregnation with Ir(COD)(acac) in MeOH followed by reduction in H$_2$ at 400 °C, obtaining the hybrid catalyst (0.04 wt% Ir uptake).[29]

Non-destructive analysis of the hybrid catalysts as-synthesized using IR (Fig. S13) or XRD (Fig. S14) was inconclusive due to the small influence of the surface modification on the bulk spectra. For this reason, physicochemical and spectroscopic characterizations were carried out after ball-milling the catalysts into a powder. Nitrogen physisorption reveals a slight increase in specific surface area from 1.0 m^2 g^{-1} of the unmodified glass to 4.9 m^2 g^{-1} for Ru@pBINAP/G, 3.3 m^2 g^{-1} for Ir@PyrTerpy/G and 4.2 m^2 g^{-1} for Ir@CTF/G. This change exemplifies the formation of additional, high surface area structures of the target polymer networks attached to the glass shape precursor. Thermogravimetric analysis (TGA) in N$_2$ reveals a mass loss of less than 1% up to 850 °C (Fig. S15). As previous studies on comparable polymers revealed thermal stabilities up to 400 °C, this observation is best explained by the small mass fraction of the polymer

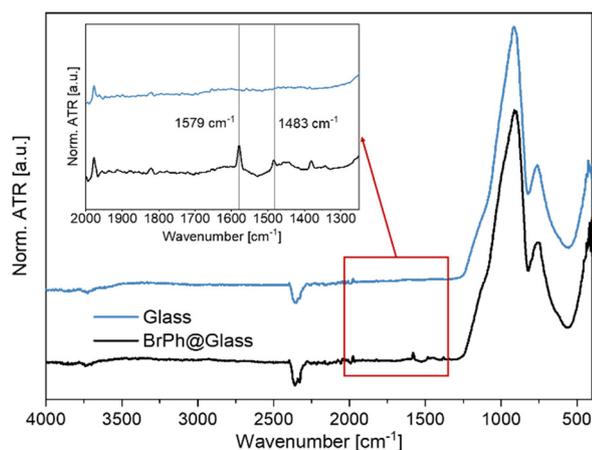**2132** | *Catal. Sci. Technol.*, 2026, **16**, 2129–2138

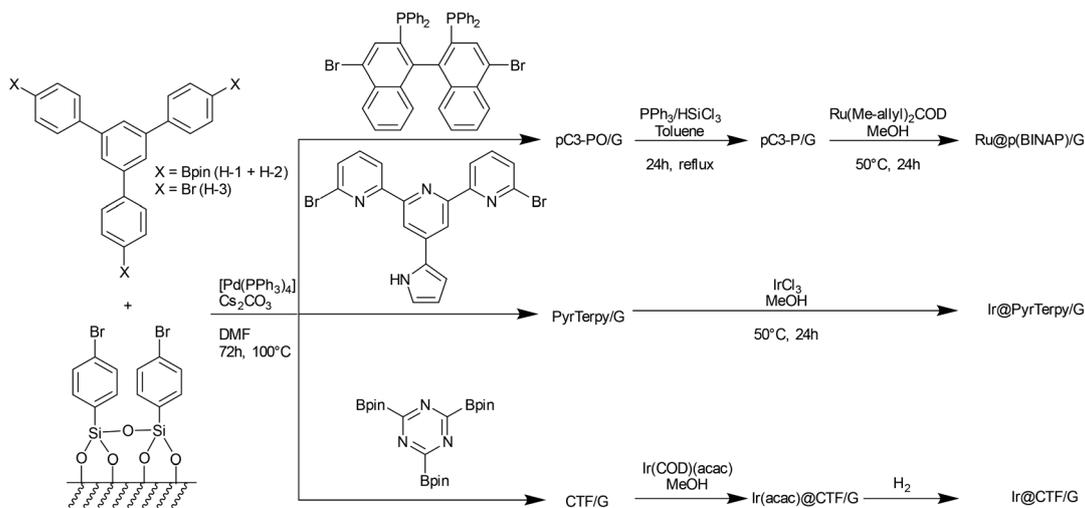This journal is © The Royal Society of Chemistry 2026

Fig. 6 Cross coupling-based synthesis methods for BINAP-, terpyridine- and CTF-based hybrid catalyst materials.

compared to the even more temperature stable glass precursor.[55,56,59] At the same time, this underlines how little polymer is required to both significantly increase the SSA of the catalyst material and to successfully uptake metal. The morphology of the resulting hybrid materials was investigated using scanning electron microscopy/energy dispersive X-ray spectroscopy (SEM/EDX) (Fig. 7 and 8 and S10–S12). The SEM images of the hybrid catalysts reveal a distribution of the organic material over the surface of the glassy support. The polymers primarily fill the free pores of the inorganic carrier and form an interpenetrating network. The close interaction of the polymers with glass the surface also suggests, as was verified using the model studies above, that the polymers are also chemically bound to the surface. Differences in the polymer morphology between the three catalysts can be observed in SEM. While Ru@pBINAP/G and Ir@CTF/G present as net-like structures that cover the entire glass surface, the terpyridine-based system Ir@PyrTerpy/G forms a rather rigid, block-like structure with large cracks in the surface. EDX analysis of Ru@pBINAP/G reveals the presence of P as well as Ru atoms inside the organic domain with a concurrent absence in the glass-domain, in line with metal loaded BINAP moieties. X-ray diffractograms of the hybrid catalysts are dominated by the spectrum of the amorphous glass support (Fig. S12). Analysis of Ru@pBINAP/G using ^{31}P NMR spectroscopy after ball-milling reveals signals at −16 ppm, assigned to reduced phosphines as well as at 24 ppm, assigned to phosphine oxides (Fig. 9).

Table 1 SSAs and measured metal loading for glass and the hybrid catalysts

Entry	SSA [$m^2 g^{-1}$]	Measured metal loading [wt%]
Glass	1.0	—
Ru@pBINAP/G	4.9	0.065 ± 0.002
Ir@PyrTerpy/G	3.3	0.087 ± 0.006
Ir@CTF/G	4.2	0.040 ± 0.008

Batch catalysis and recycling

As proof of concept for this novel class of materials, the three hybrid catalyst materials were subsequently investigated for their activity in batch decomposition reactions experiments of 10 wt% FA at 160 °C utilizing circular thin porous supported catalyst pellets (1 mm thickness by 10 mm diameter) following a previously described procedure.[26] As expected, shaping the catalytically active metals via the hybrid catalysts led to a reduced TOF in comparison to their polymeric analogs (Fig. 10, top). This is attributed to the added complexity of the mass transfer into the pores of the inorganic support material in addition to the diffusion into the SMC itself. Ru@pBINAP/G exhibits a TOF of up to 29 200 h^{-1} (63% of SMC) and a CO-concentration of 330 ppm. A study on the recycling of Ru@pBINAP/G revealed significantly improved handling of the catalyst material, albeit a decrease in catalytic activity was observed after each cycle (Fig. 10, bottom). The TOF decreased to 19 100 h^{-1} with a concurrent decrease of CO-concentration to 450 ppm over four catalyst cycles. The lower relative decrease in TOF is attributed to decreased loss of active catalyst material due to the simplified recycling of the hybrid catalysts. The increase in CO-concentration is likely caused by oxidation of the phosphines. In contrast, the terpyridine-based material exhibited a more pronounced decrease in activity from the free SMC of 40 250 h^{-1} and a CO-concentration of 208 ppm down to 11 000 h^{-1} with an improved CO-concentration of 99 ppm for Ir@PyrTerpy/G at 160 °C. The CTF-based material Ir@CTF/G exhibited the lowest TOF of 8700 h^{-1} and highest CO-concentration of 1830 ppm as SMC, and accordingly also as hybrid catalyst with a TOF of 6300 h^{-1} and a CO-concentration of 3200 ppm.

Continuous FAD in a plug-flow reactor

As both the Ru- and the Ir-SMC-based catalysts exhibited distinct advantages in terms of activity and CO-concentration,
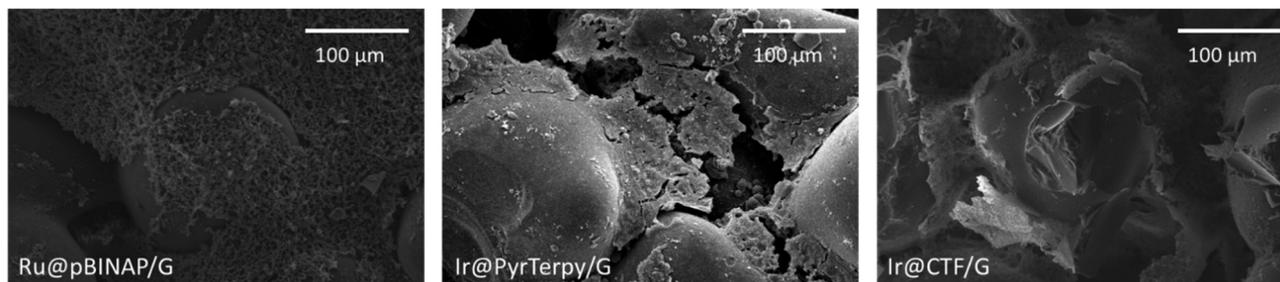
Fig. 7 Scanning electron microscopy images of the hybrid catalysts Ru@pBINAP/G (left), IrCl₃@PyrTerpy/G (middle), Ir(acac)@CTF/G (right).

respectively, a further investigation of the long-term stability and technical applicability of Ru@pBINAP/G and Ir@PyrTerpy/G was carried out in a plug flow reactor (Fig. 11). The developed procedure for catalysts synthesis was successfully scaled up to cylindrical porous glass supports with a diameter of 10 mm and a length of 450 mm, representing a scale up in catalyst volume of 450×. To ensure safe operability and catalyst utility the pressure drop over the hybrid catalysts was characterized prior to the FAD experiments by variation of argon flow over the shaped catalyst materials (Fig. S16). At 60 mL min⁻¹ Ar, the glass support exhibited a pressure loss of 0.60 mbar cm⁻¹, Ir@PyrTerpy/G of 20 mbar cm⁻¹ and Ru@pBINAP/G of 31 mbar cm⁻¹, demonstrating a viable operation window for the FAD setup. Nonetheless, implementation in larger scale setups requires further optimization of the catalyst geometry to avoid the significant pressure drops detected. The turnover frequency and TON were calculated using the following equations:

$$\text{TOF}_{\text{Conti}} = \frac{n(\text{FA})}{n(\text{Metal}) \times \tau} = \frac{\dot{n}(\text{FA})}{n(\text{Metal})} = \frac{\dot{m}(\text{FA})}{M(\text{FA}) \times n(\text{Metal})}$$
$$= \frac{\dot{V}(\text{FA}) \times \rho(\text{FA}_{\text{aq.}}) \times X(\text{FA})_{\text{HPLC}} \times S(\text{Dehy.})}{M(\text{FA}) \times n(\text{Metal})}$$

$$\text{TON} = \frac{n(\text{FA})_{\text{total}}}{n(\text{Metal})} = \sum_i \text{TOF}_{\text{Conti},i} \times t_i$$
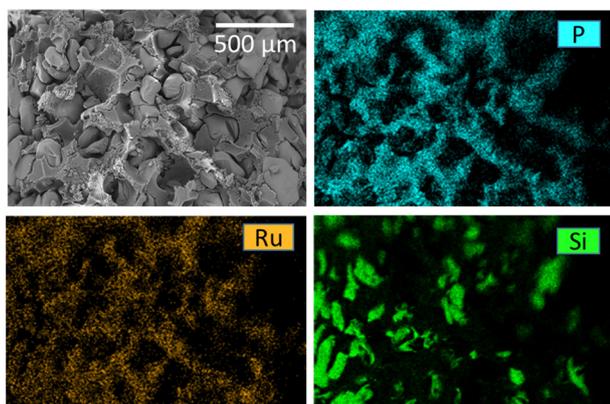
τ = contact time (min)

$X(\text{FA})_{\text{HPLC}}$ = conversion of FA as determined by HPLC analysis (—)

$\rho(\text{FA}_{\text{aq.}})$ = density of aqueous formic acid solution (g mL⁻¹)

$\dot{V}(\text{FA})$ = volumetric flow of FA set using HPLC pump (ml min⁻¹)

$S(\text{Dehy.})$ = selectivity towards FA dehydrogenation.

As selectivity in all cases was determined to be above 99.9%,

$S(\text{Dehy.})$ is approximated by 1.

The pressure of the reactor was set to 5 bar during FAD reactions, while the flowrates of the aqueous FA and the reaction temperature were screened. The CO-concentration was determined by offline gas chromatography and the conversion of the reaction determined from the liquid phase by offline HPLC and metal leaching by ICP-MS. Ru@pBINAP/G and Ir@PyrTerpy/G were investigated in continuous operation with 10.0 wt% FA. To this end, after an induction phase at 160 °C, the temperature and contact time of the system was screened. Therefore, the flow rates of aqueous FA were varied between 1.0 and 2.5 mL min⁻¹ at 100 °C, 130 °C and 160 °C respectively and the conversion and CO-concentration were determined (Fig. 12). Initially, Ru@pBINAP/G was investigated. To investigate if deactivation occurred during the reaction, the initial conversion at 160 °C was compared to the conversion at the end of the catalyst run. No significant deactivation could be observed until the TON of 11 000 was reached after 300 min. After the catalyst conditioning, the temperature was lowered to 100 °C and the
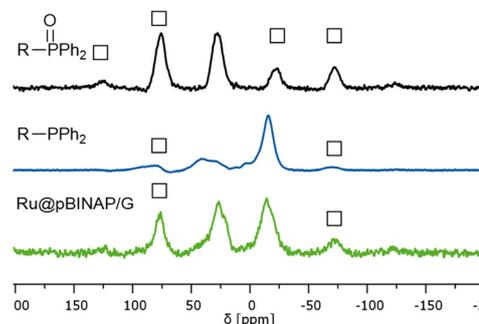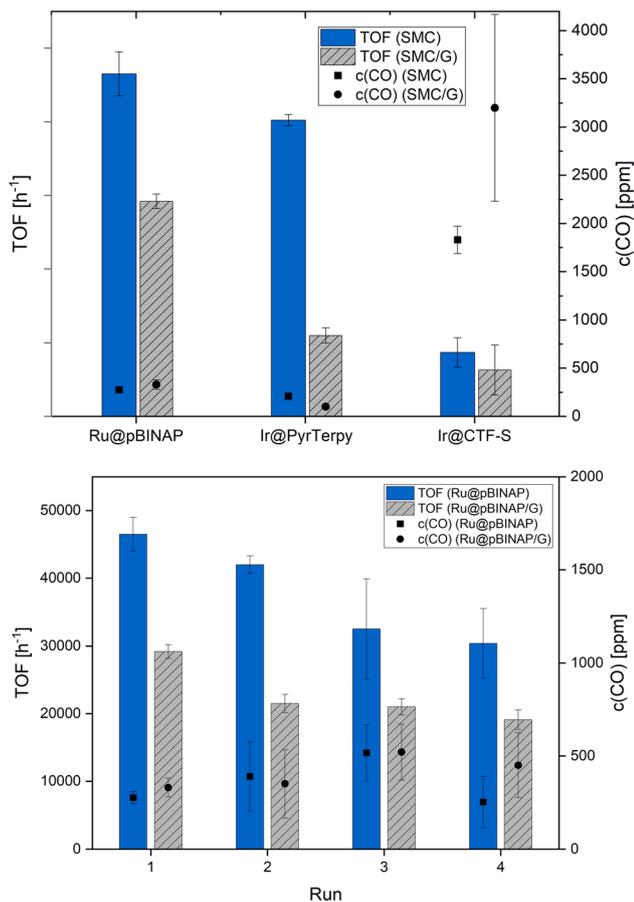

**Fig. 8** SEM/EDX element map of Ru@pBINAP/G.

Fig. 9 ³¹P NMR spectra at 10 kHz of unreduced p(BINAPO) (top), of reduced p(BINAP) (middle) and the product of the reduction of the hybrid material Ru@pBINAP/G (bottom). Squares mark spinning sidebands.

Fig. 10 TOFs and CO concentrations for Ru@pBINAP/G, Ir@PyrTerpy/G and Ir@CTF/G in comparison to the SMC catalysts in the batchwise decomposition of 10 wt% aqueous FA at 160 °C (top). Recycling experiments of Ru(MA)$_2$@p(BINAP) and Ru@pBINAP/G (bottom).
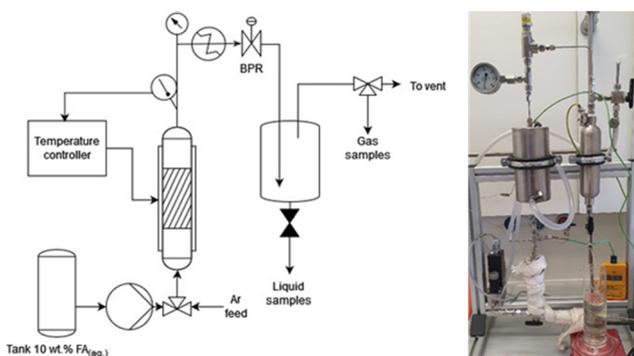
Fig. 11 Left: Schematic of continuous reactor for FAD. Right: Picture of PFR.

contact time set to 1.4 min (1.0 mL min^{-1} FA). Even at relatively low temperatures, a H$_2$ productivity ($\dot{V}$(H$_2$)) of 44 mL min^{-1} with a CO-concentration of 380 ppm was achieved. With increasing flow rate and thus decreasing contact time at a constant temperature, the conversion of the reaction decreased, while CO-concentration remained constant throughout the experiment. ICP-MS reveals a Ru metal loss
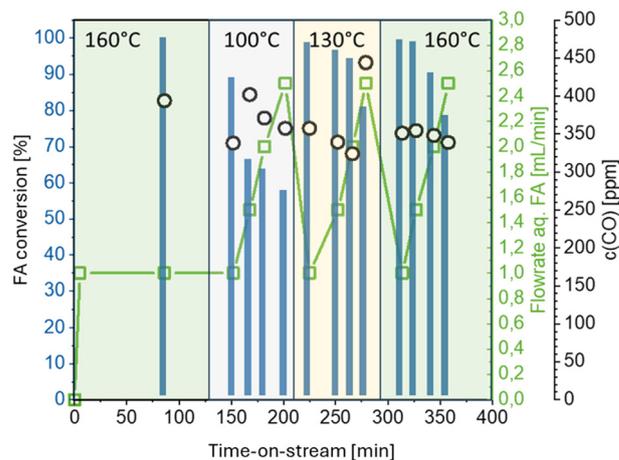

Fig. 12 Exemplary reaction scheme for continuous FAD in the PFR with the hybrid catalyst Ru@pBINAP/G.

less than 0.33 ± 0.19 mol%. This extremely low leaching, contrasted by an observable catalyst deactivation at higher TON, highlights the fact that even the products of the Ru deactivation pathway preferably remain on the catalyst surface, resulting in exceptional metal retention, which is one of the key drivers of cost in industrial application.

Evaluation of the total amount of hydrogen formed under the various conditions reveals a temperature of 130 °C with a flow rate of 2.5 mL min^{-1} as the optimum operating point. At this point, the highest hydrogen yield of 93 mL min^{-1} with a CO-concentration of 476 ppm was achieved (Fig. 13). The reaction at 160 °C exhibits a CO-concentration of 456 ppm with a H$_2$ productivity of 90 mL min^{-1}. Due to this, operation at 130 °C is advantageous for technical applications due to the improved energy efficiency resulting from the lower reaction temperature.

Similarly, the properties of the terpyridine-based hybrid catalyst Ir@PyrTerpy/G were also investigated in continuous operation. Up until a TON of 40 000 was reached, no significant deactivation was observable, again highlighting the exceptional stability of the system (Fig. S17). After the induction phase, the reaction temperature and FA flow rate were varied akin to Ru@pBINAP/G. At 100 °C and 1.0 mL min^{-1} FA flowrate, Ir@PyrTerpy/G already exhibits an H$_2$
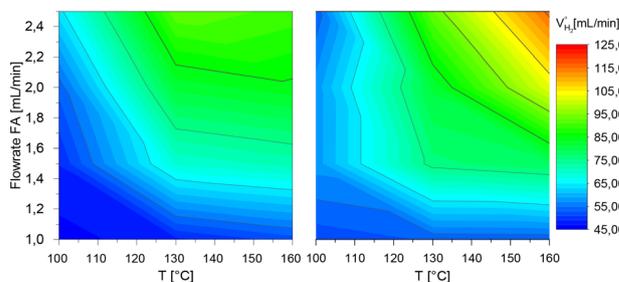
Fig. 13 Evaluation of the real H$_2$ yields at different temperatures and FA flow rates during continuous FAD experiment with Ru@pBINAP/G (left) and Ir@PyrTerpy/G (right) in the PFR.

This journal is © The Royal Society of Chemistry 2026

Catal. Sci. Technol., 2026, **16**, 2129–2138 | **2135**

productivity of 53 mL min^{-1} with a much better CO-concentration of just 58 ppm. Hydrogen productivity further increased up to 115 mL min^{-1} at 75 ppm CO at 160 °C (Fig. 13). This corresponds to a TOF of 11 000 h^{-1}, analogous to the batch experiments. ICP-MS reveals an Ir leaching of 0.38 ± 0.27%, revealing that both SMCs enable exceptional metal retention.

Analysing and comparing the CO-concentration at different H$_2$ productivities and temperatures for Ru@pBINAP/G and Ir@PyrTerpy/G (Fig. 14), it can be noted that the target CO-concentration is not achieved by the BINAP-based system Ru@pBINAP/G under any of the reaction conditions investigated. Ir@PyrTerpy/G, on the other hand, has a large temperature and productivity window at which H$_2$ can be released with sufficiently low CO-concentration. The necessary purity of less than 100 ppm CO in the produced H$_2$ for the utilization of more CO-resistant proton exchange membrane (PEM) anodes such as Pt–WO$_3$/C is achieved throughout all of the reaction parameters screened for Ir@PyrTerpy/G.[60] Further optimization to the catalyst preparation and the reaction parameters to decrease the amount of CO below 10 ppm is required to allow the use of product gas in integrated energy storage facilities with platinum-based PEM fuel cells.[5,61]

Conclusion

In this paper, a novel platform for the synthesis of shaped hybrid composite catalyst materials was developed, enabling a step towards industrial application of solid molecular catalysts. A shaped porous glass monolith grafted with a tailor-made phenylsiloxane was utilized to covalently bind organic ligand containing polymers to the surface. In this manner, BINAP-, terpyridine- and triazine-containing shaped inorganic–organic hybrid catalysts for the formic acid decomposition reaction could be obtained after impregnation with 0.1 wt% Ru or Ir. Their catalytic activity, recyclability and ease of handling were verified in batch experiments with observed TOFs of up to 29 200 h^{-1} and selectivities of up to 330 ppm for a BINAP containing hybrid catalyst, and TOFs up to 11 000 h^{-1} and CO contents below 100 ppm for the terpyridine system, proving superior over the CTF-analogue. While the BINAP-system showed particularly promising activities in batch experiments, its limited stability proved challenging in subsequent, scaled-up continuous reactions employing a plug-flow reactor. In contrast, the highest H$_2$ productivities of up to 115 mL min^{-1}, no deactivation and good selectivity at 75 ppm CO could be observed utilizing the exceptionally stable terpyridine-based catalyst Ir@PyrTerpy/G at 160 °C. Only very low leaching (0.38%) of the metal precursors could be observed under continuous operation for both systems, highlighting the exceptional metal retention of such catalysts, with important implications regarding costs en route to practical application.

Author contributions

S. Seidel: conceptualization, methodology, validation, investigation, data curation, writing – original draft, writing – review & editing, visualization. K. V. A. Birkelbach: resources, writing – review & editing. J. Mädicke: investigation. P. J. C. Hausoul: conceptualization, writing – review & editing, supervision. M. Pilaski: funding acquisition, supervision, resources. R. Palkovits: funding acquisition, supervision, project administration.

Conflicts of interest

There are no conflicts to declare.

Data availability

The data supporting this article have been included as part of the supplementary information (SI).

Supplementary information: additional IR-spectra, XRD results, synthetic methodology, catalytic procedure. See DOI: https://doi.org/10.1039/d5cy01382h.
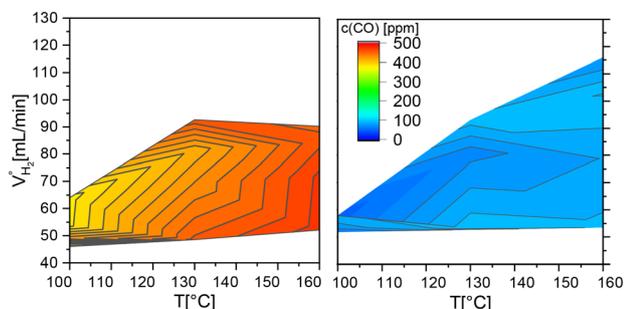
Acknowledgements

Fig. 14 Concentration of side product CO at different H$_2$ productivities and reaction temperatures of Ru@pBINAP/G (left) and Ir@PyrTerpy/G (right).

Notes and references

1 M. S. Prevot, V. Finelli, X. Carrier, G. Deplano, M. Cavallo, E. A. Quadrelli, J. Michel, M. H. Pietraru, C. Camp, G. Forghieri, A. Gagliardi, S. Seidel, A. Missemer, B. Reuillard, B. Centrella, S. Bordiga, M. G. Salamanca Gonzalez, V. Artero, K. V. A. Birkelbach and N. von Wolff, *Chem. Sci.*, 2024, **15**, 9054–9086.

2 M. A. Evans, C. Bono and Y. Wang, *IEEE Power Energy Mag.*, 2022, **20**, 44–54.

3 I. Tsiropoulos, W. Nijs, D. Tarvydas and P. Ruiz, *Publications Office of the European Union*, 2020, EUR 29981 EN.

4 A. Züttel, *Sci. Nat.*, 2004, **91**, 157–172.

5 K. B. Prater, *J. Power Sources*, 1994, **51**, 129–144.

6 S. C. Kelley, *Electrochem. Solid-State Lett.*, 2000, **3**, 407.

7 M. Niermann, A. Beckendorff, M. Kaltschmitt and K. Bonhoff, *Int. J. Hydrogen Energy*, 2019, **44**, 6631–6654.

8 C. Arnaiz del Pozo and S. Cloete, *Energy Convers. Manage.*, 2022, **255**, 115312.

9 N. Salmon and R. Bañares-Alcántara, *Sustainable Energy Fuels*, 2021, **5**, 2814–2839.

10 C. J. McKinlay, S. R. Turnock and D. A. Hudson, *Int. J. Hydrogen Energy*, 2021, **46**, 28282–28297.

11 W. Gan, P. J. Dyson and G. Laurenczy, *ChemCatChem*, 2013, **5**, 3124–3130.

12 L. Alrais, S. S. Gholap, I. Dutta, E. Abou-Hamad, B. W. J. Chen, J. Zhang, M. N. Hedhili, J.-M. Basset and K.-W. Huang, *Appl. Catal., B*, 2024, **342**, 123439.

13 P. Stathi, Y. Deligiannakis, G. Avgouropoulos and M. Louloudi, *Appl. Catal., A*, 2015, **498**, 176–184.

14 X. S. Zhao, X. Y. Bao, W. Guo and F. Y. Lee, *Mater. Today*, 2006, **9**, 32–39.

15 S. Hübner, J. G. de Vries and V. Farina, *Adv. Synth. Catal.*, 2016, **358**, 3–25.

16 A. Beloqui Redondo, F. L. Morel, M. Ranocchiari and J. A. van Bokhoven, *ACS Catal.*, 2015, **5**, 7099–7103.

17 D. E. De Vos, I. F. J. Vankelecom and P. A. Jacobs, in *Chiral Catalyst Immobilization and Recycling*, Leuven, Belgium, 2000, ch. 1, vol. 1, pp. 1–17.

18 C. M. Halliwell and A. E. G. Cass, *Anal. Chem.*, 2001, **73**, 2476–2483.

19 N. Kumagai and M. Shibasaki, *Isr. J. Chem.*, 2017, **57**, 270–278.

20 M. Rohr, M. Günther, F. Jutz, J.-D. Grunwaldt, H. Emerich, W. v. Beek and A. Baiker, *Appl. Catal., A*, 2005, **296**, 238–250.

21 C.-D. Wu and M. Zhao, *Adv. Mater.*, 2017, **29**, 1605446.

22 P. Kluson, P. Krystynik, P. Dytrych and L. Bartek, *React. Kinet., Mech. Catal.*, 2016, **119**, 393–413.

23 S. El Mourabit, M. Guillot, G. Toquer, J. Cambedouzou, F. Goettmann and A. Grandjean, *RSC Adv.*, 2012, **2**, 10916–10924.

24 A. V. Bavykina, M. G. Goesten, F. Kapteijn, M. Makkee and J. Gascon, *ChemSusChem*, 2015, **8**, 809–812.

25 P. J. C. Hausoul, C. Broicher, R. Vegliante, C. Göb and R. Palkovits, *Angew. Chem., Int. Ed.*, 2016, **55**, 5597–5601.

26 A. Kann, H. Hartmann, A. Besmehn, P. J. C. Hausoul and R. Palkovits, *ChemSusChem*, 2018, **11**, 1857–1865.

27 R. Sun, A. Kann, H. Hartmann, A. Besmehn, P. J. C. Hausoul and R. Palkovits, *ChemSusChem*, 2019, **12**, 3278–3285.

28 A. V. Bavykina, A. I. Olivos-Suarez, D. Osadchii, R. Valecha, R. Franz, M. Makkee, F. Kapteijn and J. Gascon, *ACS Appl. Mater. Interfaces*, 2017, **9**, 26060–26065.

29 A. Iemhoff, M. Vennewald, J. Artz, C. Mebrahtu, A. Meledin, T. E. Weirich, H. Hartmann, A. Besmehn, M. Aramini, F. Venturini, F. W. Mosselmans, G. Held, R. Arrigo and R. Palkovits, *ChemCatChem*, 2022, **14**, e202200179.

30 A. Kann, H. Hartmann, A. Besmehn, P. J. C. Hausoul and R. Palkovits, *ChemSusChem*, 2018, **11**, 1857–1865.

31 S. Yuan, X. Li, J. Zhu, G. Zhang, P. Van Puyvelde and B. Van der Bruggen, *Chem. Soc. Rev.*, 2019, **48**, 2665–2681.

32 G. H. Gunasekar, H. Kim and S. Yoon, *Sustainable Energy Fuels*, 2019, **3**, 1042–1047.

33 M. Rose, *ChemCatChem*, 2014, **6**, 1166–1182.

34 L. Huang, J. Yang, Y. Zhao, H. Miyata, M. Han, Q. Shuai and Y. Yamauchi, *Chem. Mater.*, 2023, **35**, 2661–2682.

35 E. B. Anderson and M. R. Buchmeiser, *ChemCatChem*, 2012, **4**, 30–44.

36 E. Ruiz-López, M. Ribota Peláez, M. Blasco Ruz, M. I. Domínguez Leal, M. Martínez Tejada, S. Ivanova and M. Á. Centeno, *Materials*, 2023, **16**, 472.

37 P. Sponholz, D. Mellmann, H. Junge and M. Beller, *ChemSusChem*, 2013, **6**, 1172–1176.

38 K. Sawahara, S. Tanaka, T. Kodaira, R. Kanega and H. Kawanami, *ChemSusChem*, 2024, **17**, e202301282.

39 T. Pilhofer, *Chem. Ing. Tech.*, 1984, **56**, 299–305.

40 J. J. Cras, C. A. Rowe-Taitt, D. A. Nivens and F. S. Ligler, *Biosens. Bioelectron.*, 1999, **14**, 683–688.

41 H.-M. Kao, C.-H. Liao, T.-T. Hung, Y.-C. Pan and A. S. T. Chiang, *Chem. Mater.*, 2008, **20**, 2412–2422.

42 N. A. Green, A. A. Meharg, C. Till, J. Troke and J. K. Nicholson, *Appl. Environ. Microbiol.*, 1999, **65**, 4021–4027.

43 D. Qiu, S. Li, G. Yue, J. Mao, B. Xu, X. Yuan and F. Ye, *Tetrahedron Lett.*, 2021, **85**, 153478.

44 K. Hara, S. Akahane, J. W. Wiench, B. R. Burgin, N. Ishito, V. S. Y. Lin, A. Fukuoka and M. Pruski, *J. Phys. Chem. C*, 2012, **116**, 7083–7090.

45 M. C. Capel-Sanchez, L. Barrio, J. M. Campos-Martin and J. L. Fierro, *J. Colloid Interface Sci.*, 2004, **277**, 146–153.

46 E. Arellano-Archán, M. Esneider Alcalá, O. E. Vega-Becerra, T. E. Lara-Ceniceros and J. Bonilla-Cruz, *ACS Omega*, 2018, **3**, 16934–16944.

47 W. Zierkiewicz, D. Michalska and T. Zeegers-Huyskens, *J. Phys. Chem. A*, 2000, **104**, 11685–11692.

48 S. M. Chemtob, G. R. Rossman and J. F. Stebbins, *Am. Mineral.*, 2012, **97**, 203–211.

49 Y. Takeuchi and T. Takayama, in *The Chemistry of Organic Silicon Compounds*, 1998, pp. 267–354.

This journal is © The Royal Society of Chemistry 2026

Catal. Sci. Technol., 2026, **16**, 2129–2138 | 2137

50 M. Torres-Carrasco, J. G. Palomo and F. Puertas, *Mater. Constr.*, 2014, 64.

51 J. Ramkumar, V. Sudarsan, S. Chandramouleeswaran, V. K. Shrikhande, G. P. Kothiyal, P. V. Ravindran, S. K. Kulshreshtha and T. Mukherjee, *J. Non-Cryst. Solids*, 2008, **354**, 1591–1597.

52 D. Möncke, M. Dussauze, E. I. Kamitsos, C. P. E. Varsamis and D. Ehrt, *Phys. Chem. Glasses*, 2009, **50**, 229–235.

53 D. Möncke, D. Ehrt, C.-P. E. Varsamis, E. I. Kamitsos and A. G. Kalampounias, *Phys. Chem. Glasses*, 2006, **47**, 133–137.

54 E. I. Kamitsos, A. P. Patsis, M. A. Karakassides and G. D. Chryssikos, *J. Non-Cryst. Solids*, 1990, **126**, 52–67.

55 S. Seidel, I. Kappel, C. Weidenthaler, P. J. C. Hausoul and R. Palkovits, *J. Catal.*, 2024, **438**, 115712.

56 K. V. A. Birkelbach, H. Hartmann, A. Besmehn, A. Meledin, I. Kappel, P. J. C. Hausoul and R. Palkovits, *EES Catal.*, 2025, **3**, 701–711.

57 D. Ditz, N. M. Sackers, F. Müller, M. Zobel, S. Bergwinkl, P. Nuernberger, L. S. Häser, S. Brettschneider, F. M. Wisser, C. Bannwarth and R. Palkovits, *Green Chem.*, 2024, **26**, 3397–3405.

58 D. Hérault, D. H. Nguyen, D. Nuel and G. Buono, *Chem. Soc. Rev.*, 2015, **44**, 2508–2528.

59 J. C. Baums, I. Kappel, A. Meise, M. Heggen, C. Weidenthaler, P. J. C. Hausoul and R. Palkovits, *ChemCatChem*, 2025, **17**, e202402048.

60 K. Y. Chen, Z. Sun and A. C. C. Tseung, *Electrochem. Solid-State Lett.*, 1999, **3**, 10.

61 J. J. Baschuk and X. Li, *Int. J. Energy Res.*, 2001, **25**, 695–713.

2138 | *Catal. Sci. Technol.*, 2026, **16**, 2129–2138

This journal is © The Royal Society of Chemistry 2026